Fermi surface of MoO_2 studied by angle-resolved photoemission spectroscopy, de Haas–van Alphen measurements, and electronic structure calculations

Judith Moosburger-Will, Jörg Kündel, Matthias Klemm, and Siegfried Horn
Experimentalphysik II, Institut für Physik, Universität Augsburg, D-86135 Augsburg, Germany

Philip Hofmann
Institute for Storage Ring Facilities (ISA) and Interdisciplinary Nanoscience Center (iNANO), University of Aarhus, DK-8000 Aarhus C, Denmark

Udo Schwingenschlögl
ICCMP, Universidade de Brasília, 70904-970 Brasília, DF, Brazil and Theoretische Physik II, Institut für Physik, Universität Augsburg, D-86135 Augsburg, Germany

Volker Eyert*
Center for Electronic Correlations and Magnetism, Institut für Physik, Universität Augsburg, D-86135 Augsburg, Germany
(Received 10 December 2008; published 16 March 2009)

A comprehensive study of the electronic properties of monoclinic MoO_2 from both an experimental and a theoretical point of view is presented. We focus on the investigation of the Fermi body and the band structure using angle-resolved photoemission spectroscopy, de Haas–van Alphen measurements, and electronic structure calculations. For the latter, the full-potential augmented spherical wave method has been applied. Very good agreement between the experimental and theoretical results is found. In particular, all Fermi surface sheets are correctly identified by all three approaches. Previous controversies concerning additional holelike surfaces centered around the Z and B points could be resolved; these surfaces were artifacts of the atomic-sphere approximation used in the old calculations. Our results underline the importance of electronic structure calculations for the understanding of MoO_2 and the neighboring rutile-type early transition-metal dioxides. This includes the low-temperature insulating phases of VO_2 and NbO_2, which have crystal structures very similar to that of molybdenum dioxide and display the well-known prominent metal-insulator transitions.

DOI: 10.1103/PhysRevB.79.115113 PACS number(s): 71.20.−b, 75.25.+z, 75.10.Pq, 75.50.Ee

I. INTRODUCTION

The metal-insulator transitions of the early transition-metal oxides have been attracting a lot of attention for decades. In particular, since the first report by Morin,[1] much interest has centered on the cornerstone materials V_2O_3 and VO_2. This is mainly due to the fact that these compounds display first-order phase transitions with very narrow hystereses of only few kelvin and strong changes in the conductivity of several orders of magnitude, making them promising candidates for applications. Interestingly, the transitions of both compounds are accompanied by characteristic structural changes, which initiated a discussion about the driving forces. Disputes were about the questions whether the transitions are driven predominantly by structural instabilities of the parent corundum and rutile structure, respectively, or else by strong electronic correlations. Nowadays, the importance of the latter is widely accepted. However, despite intense work, the questions concerning the origins of the respective transitions have not yet been satisfactorily answered.

In VO_2, the metal-insulator transition occurs at 340 K and is connected with a structural change from the rutile structure to a distorted monoclinic structure. The latter is characterized by (i) pairing of the metal atoms within chains parallel to the rutile **c** axis and (ii) their lateral antiferroelectric zigzag like displacement.[2,3] Electronic states near the Fermi energy are mainly of V $3d$ t_{2g} character. They fall into the $d_\parallel$ band, which mediates V-V overlap along the metal chains, and the remaining e_g^π bands.[4] At the transition, splitting of the $d_\parallel$ band and upshift of the e_g^π bands due to increased metal-oxygen overlap produce a finite band gap. Controversial discussions addressed the origin of the $d_\parallel$ splitting, which was assigned either to the metal-metal dimerization or to increased electronic correlations resulting from the reduced screening by the e_g^π electrons.[4–9] State-of-the-art electronic structure calculations gave strong hints at a structural instability but were not able to reproduce the insulating gap due to the shortcomings of the local density approximation (LDA).[10–12] Only recently, LDA+dynamical mean field theory (DMFT) calculations have demonstrated that the metal-insulator transition may be regarded as a correlation-assisted Peierls-type transition.[13]

Remarkably, the structural distortions occurring at the transition of VO_2 are characteristic of most of the neighboring d^1, d^2, and d^3 transition-metal dioxides. In particular, the metallic oxides MoO_2, WO_2, TcO_2, and α-ReO_2 all display the above-mentioned metal-metal pairing as well as the lateral displacement and crystallize in the same monoclinic structure as low-temperature VO_2.[14] This crystal structure is displayed in Fig. 1, which allows us to identify both the pairing and the lateral displacement of the metal atoms.

In contrast to the above-mentioned metallic d^2 and d^3 members, the d^1 compound NbO_2, like VO_2, undergoes

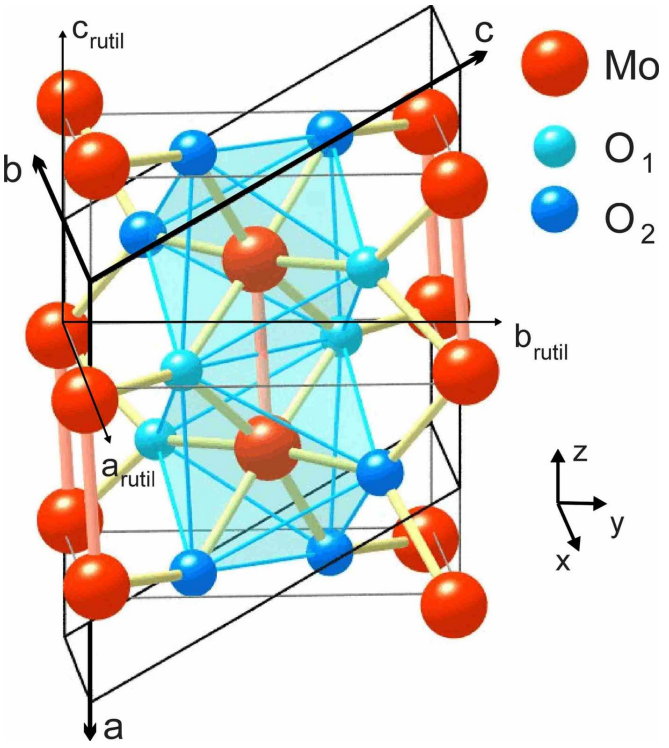

FIG. 1. (Color online) Monoclinic crystal structure of MoO_2. The dimerized metal pairs are highlighted by thick bonds.

a metal-insulator transition (at 1081 K) and a simultaneous structural transition from rutile to a distorted variant having a body-centered-tetragonal (bct) lattice.[15,16] However, despite the differences in long-range order, the local deviations from the rutile structure are the same as in VO_2, i.e., the niobium atoms dimerize and experience lateral displacements at the transition.[17–19]

Despite of the strong interest in the metal-insulator transition of VO_2, attempts at understanding the origin of the common structural characteristics are very rare. Indeed, any theory aiming at the metal-insulator transition of VO_2 would be incomplete without proper account of the local structural distortions of all the rutile-related transition-metal dioxides. In order to close the apparent gap, we have started a systematic investigation especially on VO_2, NbO_2, and MoO_2 already a decade ago, which by now provides a unified picture.[11,12,20,21]

Interest in MoO_2 was especially motivated by the metallic nature of this material, the reduced localization of the $4d$ electrons as compared to the $3d$ electrons of VO_2, and the rather small effective mass, which is similar to the free-electron mass.[22–24] These facts point to a rather weak influence of electronic correlations. Indeed, electronic structure calculations for MoO_2 show a large bonding-antibonding splitting of the $d_{\|}$ bands.[11,20] Since the occupied $d_{\|}$ bands lie far below the Fermi level, a possible influence of electronic correlations in these bands would not lead to an enhanced effective mass or susceptibility. As a consequence, MoO_2 can be regarded as a "model system" for studying the origin of the structural characteristics of the early transition-metal dioxides. In addition, an extensive examination of the electronic structure of MoO_2 could help in clarifying open questions of the above-mentioned structurally related systems, in particular of the d^1 members NbO_2 and VO_2.

In a previous work, we have presented a comprehensive theoretical study of the electronic properties of MoO_2.[11,20] Electronic structure calculations using the augmented spherical wave (ASW) method, which is based on density-functional theory and LDA, were used to analyze the electronic states involved in low-energy excitations. In addition, emphasis was put on investigating the origin of the small but distinct deviations of the monoclinic crystal structure from the parent rutile structure, which for this material mainly consist of a metal-metal dimerization parallel to the rutile **c** axis. In short, we were able to show that the monoclinic structure results from what we called an embedded Peierls-type instability. This instability affects the quasi-one-dimensional Mo $4d_{\|}$ bands, which mediate the metal-metal overlap along chains parallel to the rutile **c** axis and which are embedded in a background of the remaining three-dimensionally dispersing Mo $4d\ e_g^{\pi}$, electrons, which are also designated as the π^* electrons. The validity of this scenario had been demonstrated by comparing the electronic properties calculated for the monoclinic structure with those of a properly symmetrized artificial rutile structure. In addition, we found nearly perfect agreement of our calculated results with the outcome of ultraviolet photoemission spectroscopy (PES) and x-ray absorption spectroscopy apart from an underestimation of the $d_{\|}$ band splitting by about 1 eV due to the well-known shortcomings of the LDA.[11,20]

This scenario has also been shown to explain the metal-insulator transitions of the d^1 members VO_2 and NbO_2, which likewise are subject to Peierls-type instabilities of the quasi-one-dimensional V $3d_{\|}$ bands in the embedding backgrounds of the π^* electrons.[12,21] As in MoO_2, these instabilities cause distortions of the rutile structure by the characteristic metal-metal dimerization. Due to the particular position of the Fermi energy in the d^1 compounds, the Peierls-type instabilities are then accompanied by the observed metal-insulator transitions. At the same time, the opening of the optical band gaps is supported by the lateral antiferroelectric displacements of the metal atoms, which cause an upshift of the π^* states.

Continuing our study of MoO_2, we concentrate in the present work especially on the Fermi surface and the band dispersions. A comprehensive investigation of the full Fermi body of MoO_2, as determined both experimentally and theoretically, will be presented. In particular, we turn to a comparison of the theoretical results with angle-resolved photoemission spectroscopy (ARPES) and de Haas–van Alphen (dHvA) data. In doing so, we apply a recent implementation of the augmented spherical wave method, which goes beyond the version used in our previous work by taking into account the full potential rather than the approximate muffin-tin potential. The resulting changes in the electronic states are small but important and lead to a much improved agreement of the theoretical and experimental data.

While published photoemission studies on MoO_2 focused on the angle-integrated analysis of the occupied bands,[25–28] a systematic investigation of the band dispersions and the Fermi body by angle-resolved photoemission spectroscopy seems to be still missing. In addition, existing magnetotrans-

port measurements addressed only fractions of the Fermi surface.[22–24,29–31] It is the purpose of the present work to make up for the apparent lack in experimental data and to present a comprehensive study of the electronic structure of MoO_2.

An important difference between dHvA and ARPES is that the former requires very low temperatures whereas the latter does not. This is crucial for the early transition-metal dioxides, some of which have a metal-insulator transition and thus do not show a Fermi surface at low temperatures. In the present case we have the opportunity to compare ARPES and dHvA because MoO_2 is metallic at low T. It turns out that the ARPES and dHvA results agree well, implying that ARPES will be useful to study the Fermi surfaces of the d^1 members VO_2 and NbO_2 as well.

The paper is organized as follows: while Sec. II gives an overview on the computational method and the theoretical results, Sec. III turns to a description of the ARPES and dHvA measurements and their results. The theoretical and experimental findings are subject of a comparative discussion given in Sec. IV, and Sec. V summarizes our results.

II. ELECTRONIC STRUCTURE CALCULATIONS

A. Computational method

The calculations are based on density-functional theory and the local density approximation.[32,33] They were performed using the scalar-relativistic implementation of the augmented spherical wave method (see Refs. 34 and 35 and references therein). In the ASW method, the wave function is expanded in atom-centered augmented spherical waves, which are Hankel functions and numerical solutions of Schrödinger's equation outside and inside the so-called augmentation spheres, respectively. In order to optimize the basis set, additional augmented spherical waves were placed at carefully selected interstitial sites. The choice of these sites as well as the augmentation radii was automatically determined using the sphere-geometry optimization algorithm.[36] Self-consistency was achieved by a highly efficient algorithm for convergence acceleration.[37] The Brillouin zone integrations were performed using the linear tetrahedron method with up to 518 **k** points within the irreducible wedge.[35,38]

In the present work, we used a full-potential version of the ASW method, which was implemented only very recently.[39] In this version, the electron density and related quantities are given by a spherical harmonics expansion inside nonoverlapping muffin-tin spheres. In the remaining interstitial region, a representation in terms of atom-centered Hankel functions is used.[40] However, in contrast to previous related implementations, it is sufficient to work without having to employ a so-called multiple-κ basis set, permitting a very high computational speed of the resulting scheme.

B. Results

The electronic properties of MoO_2 in the monoclinic as well as in the above-mentioned artificial rutile structure have already been discussed in much detail in our previous work.[11,20] For this reason, we will in the following concentrate on the changes coming with the consideration of the full potential rather than its muffin-tin approximation. In particular, we will investigate the changes in the electronic states near the Fermi energy.

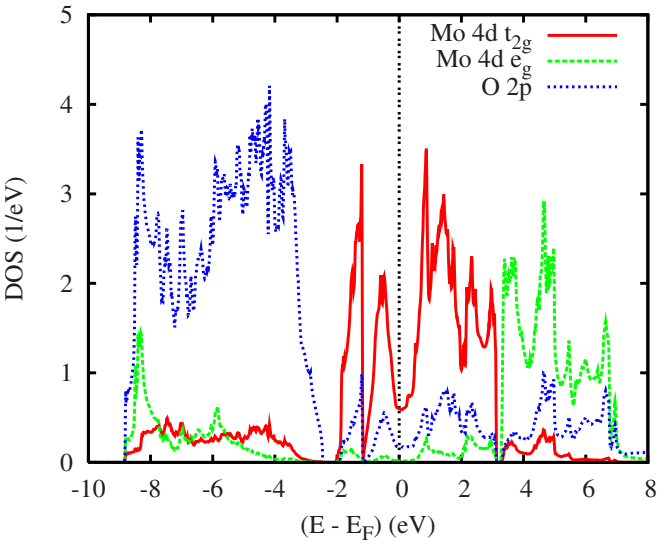

FIG. 2. (Color online) Partial DOSs.

Furthermore, since a very detailed description of the monoclinic crystal structure and its relation to the rutile structure has been given in our previous work, we will not enter a renewed discussion here. However, we refer the reader to our previous publication especially concerning the definition of the local coordinate systems to be used for the analysis of the electronic states.[11,20]

While a first account of the monoclinic crystal structure was given by Magnéli and Andersson,[41] our calculations are based on the refined data by Brandt and Skapski.[42] Hence, in contrast to our previous work,[11,20] we will exclusively deal with the measured monoclinic structure and not discuss our calculations for the related but artificial rutile structure. In addition, since there are no indications for the formation of magnetic moments in MoO_2, spin degeneracy was enforced in all calculations. The resulting partial densities of states (DOSs) are shown in Fig. 2. They look very similar to those presented previously.[11,20] In particular, we recognize the 6.5 eV wide O $2p$ bands well below the Fermi energy E_F. In contrast, the Mo $4d$ t_{2g} and e_g manifolds are found around and well above E_F. Worth mentioning is the pronounced dip of the t_{2g} partial DOS at E_F. It results from the Peierls-type instability of the $d_{x^2-y^2}$ states, which usually are designated as the $d_{\|}$ states and which mediate the metal-metal overlap along the Mo atom chains parallel to the rutile **c** axis. The splitting of these bands into bonding and antibonding branches as resulting from this Peierls-type instability is clearly visible in Fig. 3, which displays the three partial t_{2g} DOSs. In representing these partial DOSs we have used the same local coordinate system as in our previous work with the local x axis parallel to the rutile **c** axis and the local z axes pointing alternately along the [110] and [1$\bar{1}$0] directions.[11,20] In Fig. 3, we observe the strong splitting of the $d_{x^2-y^2}$ states, which no longer contribute to the metallic

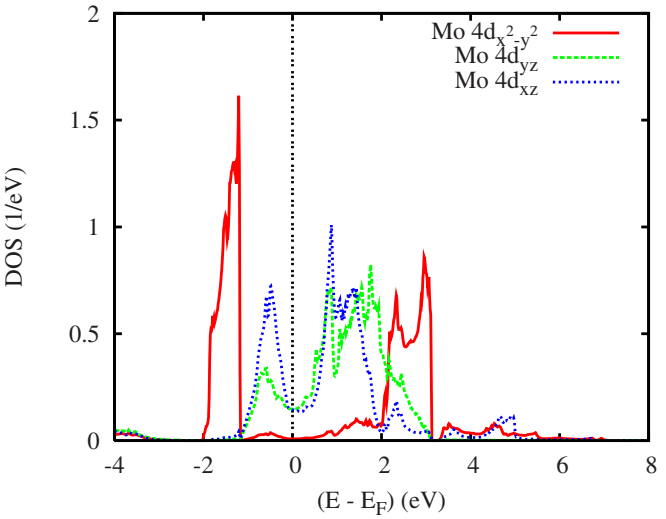

FIG. 3. (Color online) Partial Mo 4*d* t_{2g} DOS. Selection of orbitals is relative to the local rotated reference frame (see Refs. 11 and 20).

conductivity. Furthermore, due to the splitting, the low lying bonding branch is found at the lower edge of the t_{2g} group of bands and nearly separated from the higher lying d_{xz} and d_{yz} bands. The latter are commonly designated as the π^* bands.

The electronic bands along selected lines within the first Brillouin zone (Fig. 4) are displayed in Fig. 5. With the interpretation of the partial DOS at hand, we easily recognize the O 2*p* as well as the Mo 4*d* t_{2g} and e_g states in the energy intervals from −9 to −2.5 eV, −2 to +3 eV, and +3 to +7 eV, respectively. To be more detailed, we find two bands between −2 and −1 eV, which are separated from all other bands. This split-off doublet is more easily identified in Fig. 6, where we show the near-E_F bands on an expanded energy scale. According to the previous analysis, the split-off doublet is just the bonding $d_{\|}$ band. The one-dimensional behavior of the $d_{\|}$ bands is contrasted by the rather isotropic dispersion of the π^* bands. As already pointed out in our previous work, hybridization between both types of bands is rather small. In contrast, coupling of these states is only via charge conservation. For this reason, we proposed to interpret the splitting of the former in the course of the structural distortions as an embedded Peierls-type instability.[11,20]

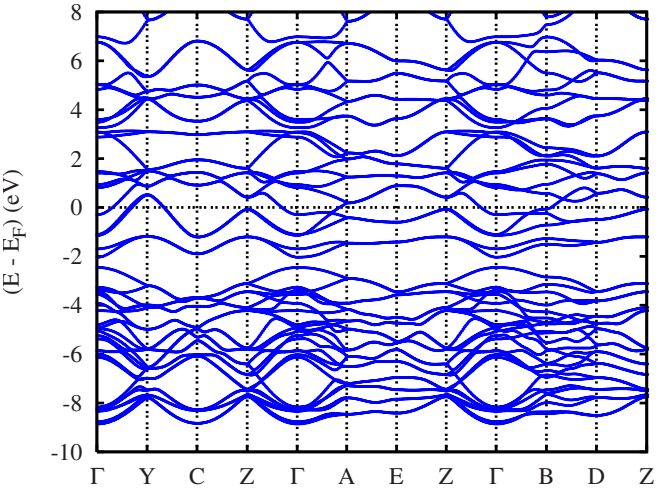

FIG. 5. (Color online) Electronic bands.

Concentrating especially on the Fermi body of monoclinic MoO_2, we complement Fig. 6 by Fig. 7, which displays cuts through the Fermi body in the **ac** plane, the **ab** plane, and perpendicular to the **a** axis as well as a three-dimensional view of the Fermi surface sheets. The Fermi body is defined by the Fermi-level crossings of the d_{xz} and d_{yz} bands. In Figs. 6 and 7, we identify three different Fermi surface sheets: two holelike surfaces near the *Y* point (sheets 1 and 2), which

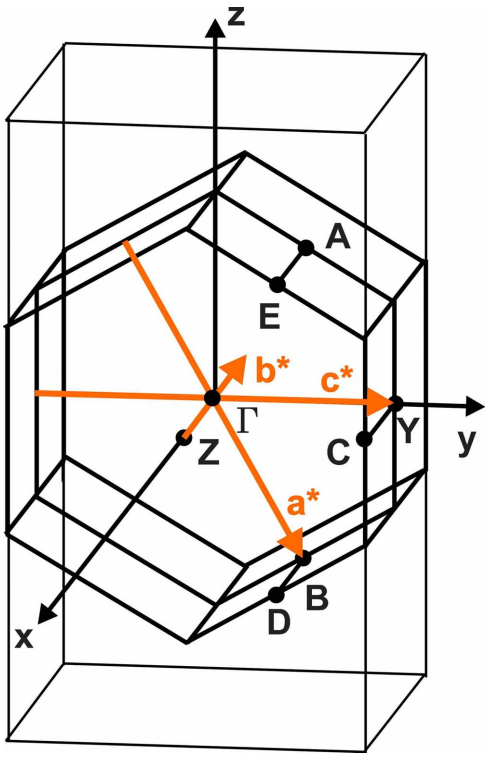

FIG. 4. (Color online) First Brillouin zone of the simple monoclinic lattice.

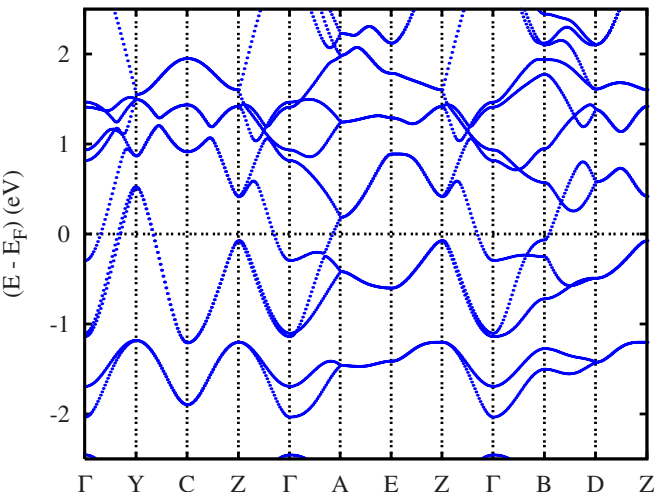

FIG. 6. (Color online) Near-E_F electronic bands on an expanded energy scale.

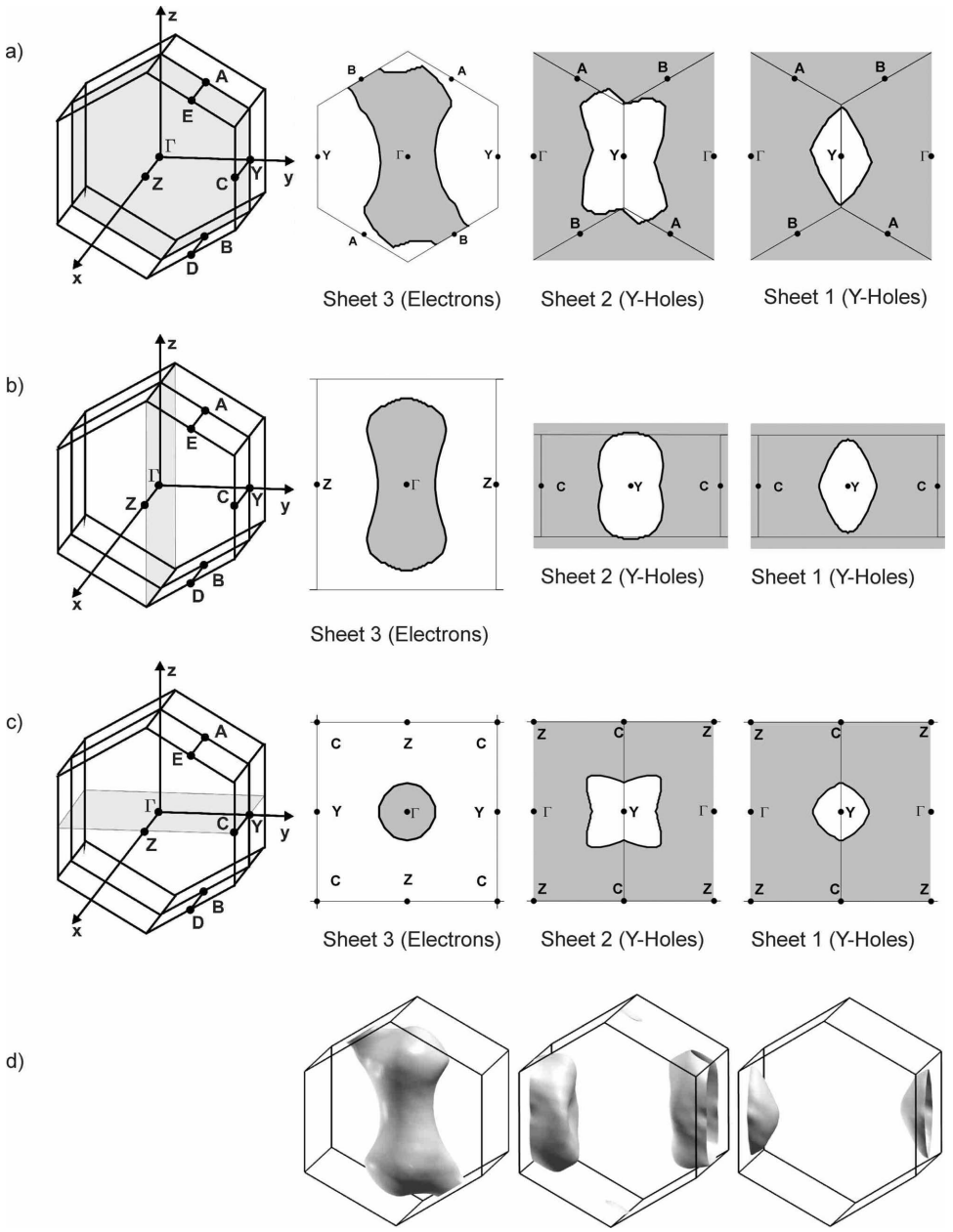

FIG. 7. Cuts through the Brillouin zone (left column) and the Fermi body (a) in the **ac** plane, (b) in the **ab** plane, and (c) perpendicular to **a** as well as (d) three-dimensional view of the three Fermi surface sheets [generated using XCRYSDEN (Ref. 43)].

occupy 9% and 2%, respectively, of the volume of the first Brillouin zone, as well as a peanut-shaped electronlike surface centered around the Γ point and occupying 11% of the Brillouin zone volume (sheet 3). The latter sheet has two loopholes near the *B* points, whereas it is closed along the direction Γ-*A*.

As already mentioned in Sec. I, use of the exact single-particle potential, i.e., of the so-called full potential, instead of its muffin-tin or atomic sphere approximation leads to important improvements. These become obvious from comparing Fig. 6 of the present work to Fig. 6 of Ref. 20. Apart from a broadening of the O 2*p* bands we find distinct differences especially at the *Z* and the *B* points. To be specific, those bands, which form the highest occupied states at these points in the present calculation, were found just above E_F in the old calculation. They generated small holelike pockets of the Fermi surface centered around these points, which were at variance with the experimental findings (see below). In contrast, in the new calculation these bands are found below E_F and the holelike pockets disappear.

Another important difference can be observed at the Γ point. The maximum binding energy of the highest occupied band of the new calculation (0.30 eV) agrees much better with the experimental value of 0.21 eV (see below) than the binding energy of the old calculation (0.43 eV). Thus, by using the full-potential ASW method, the agreement between theory and experiment is considerably improved.

III. EXPERIMENTS

A. Sample preparation and characterization

MoO_2 single crystals were grown by chemical transport using $TeCl_4$ as transport agent.[44] The crystals exhibit specu-

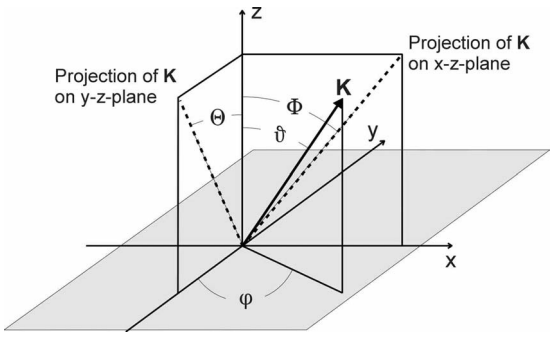

FIG. 8. Measurement geometry and definition of the emission angles in an ARPES experiment. Here, **K** is the wave vector in vacuum.

lar surfaces of a size up to 3×3 mm^2. The surface orientation was determined by x-ray diffraction (XRD). For the ARPES measurements the as-grown surfaces were cleaned *in situ* by heating to 750 °C for some minutes. The quality and cleanness of the heated single-crystal surfaces were controlled by low-energy electron diffraction (LEED) and by scanning tunneling microscopy (STM). For the dHvA measurements several rods of 3 mm length and 1.5 mm diameter were prepared. The **b** axis was the axis of rotation of the rods. The residual resistance ratios were 97 for $\mathbf{j}\|\mathbf{a}$ and 144 for $\mathbf{j}\|\mathbf{b}$.

B. Angle resolved photoemission spectroscopy (ARPES)

Experimentally, the electronic structure $E(\mathbf{k})$ was investigated by ARPES measurements using the geometry and emission angles defined in Fig. 8. Due to energy conservation the binding energy E_B of the photoelectron is determined by

$$|E_B| = h\nu - E_{\mathrm{kin}} - \phi, \tag{1}$$

where $h\nu$ is the photon energy and ϕ is the work function of the crystal. For a detailed description of the photoemission process we refer the reader to the literature.[45–48]

On passing through the crystal surface, the component of the electron wave vector parallel to the surface $\mathbf{k}_\|$ remains unchanged with

$$|\mathbf{k}_\|| = \frac{1}{\hbar}\sqrt{2mE_{\mathrm{kin}}}\sin\vartheta. \tag{2}$$

The perpendicular component $\mathbf{k}_\perp$ is, strictly spoken, not conserved in the photoemission process but it is usually possible to reconstruct its approximate value by including information about the final states of the photoemission process. If one assumes a free-electron-like final state dispersion cit-enielsen03, $k_\perp = |\mathbf{k}_\perp|$ can be calculated as

$$k_\perp = \frac{1}{\hbar}\sqrt{2m(E_{\mathrm{kin}}\cos^2\vartheta + |E_0| + \phi)}. \tag{3}$$

Here, E_0 is the inner potential of the sample as referred to E_F. While the work function ϕ can be determined experimentally, the inner potential E_0 is usually estimated from an analysis of the measured band structure. As a consequence of Eq. (3), the set of all $\mathbf{k}_\|$ vectors at a fixed photon energy describes a spherical surface in **k** space.

A Fermi vector $\mathbf{k}_F$ is defined by the Fermi-level crossing of a valence band in the corresponding direction of **k** space. As ARPES permits a complete mapping of a solid's three-dimensional band structure, the position of the Fermi-level crossings can be identified. A three-dimensional ARPES measurement can be performed by varying the emission angles and $h\nu$, causing a variation in $\mathbf{k}_\|$ and $\mathbf{k}_\perp$, respectively.

The ARPES measurements were done at the beamline SGM3 at the synchrotron ASTRID in Aarhus, Denmark. The beamline provides light in the energy range 12 eV$<h\nu<$130 eV with an energy resolution of $E/\Delta E=15\,000$.[50] The UHV chamber is equipped with an ARUPS10 electron analyzer (Vacuum Generators) with an angular resolution of 0.7° and an energy resolution of 25 meV. The analyzer is fixed on a computer controlled two-axis goniometer with an angular accuracy up to 0.2°. All ARPES data were taken at a temperature of 30 K. For the description of the measurement geometry, instead of the polar emission angle ϑ, its projections on the *xz* and *yz* planes are used (see Fig. 8). The resulting emission angles are called Φ and Θ. The direction of normal emission was determined by a careful optical alignment of the highly reflective surface using a laser.

C. ARPES results

1. (100) surface

ARPES spectra taken on the (100) surface for variation in the emission angles Φ and Θ are shown in Figs. 9(a) and 9(b), respectively. At $h\nu=19$ eV, binding energies up to 0.6 eV have been measured. In both graphs a single peak is observed, which displays a nearly parabolic dispersion. At normal emission ($\Phi=0$ and $\Theta=0$), it reaches a maximum binding energy of 0.22 eV. With increasing emission angles, both Φ and Θ, the peak approaches the Fermi level and crosses it. As will be shown later by the symmetry of the Fermi surface, the Γ point is reached at $h\nu=19$ eV. Hence, the maximum binding energy of 0.22 eV corresponds to the binding energy at the Γ point. We can thus compare the occupied bandwidth determined here directly with the binding energy of the highest occupied LDA band at the Γ point which is 0.3 eV.

Analyzing the nearly parabolic dispersion of the ARPES band, effective masses of $0.876m_e$ and $0.821m_e$ can be found for variation in the emissions angles Φ and Θ, respectively. This is in excellent agreement with Shubnikov–de Haas measurements in Ref. 24, which provided for comparable geometry an effective mass of $0.83m_e$.

2. Determination of the Fermi body

The Fermi-level crossing of the highest occupied band, defining the corresponding Fermi vector, can be identified by a strong increase in photoemission intensity at E_F. Indeed, ARPES can also provide a direct image of the Fermi surface when the photoemission intensity in a narrow energy window around the Fermi level is displayed as a function of

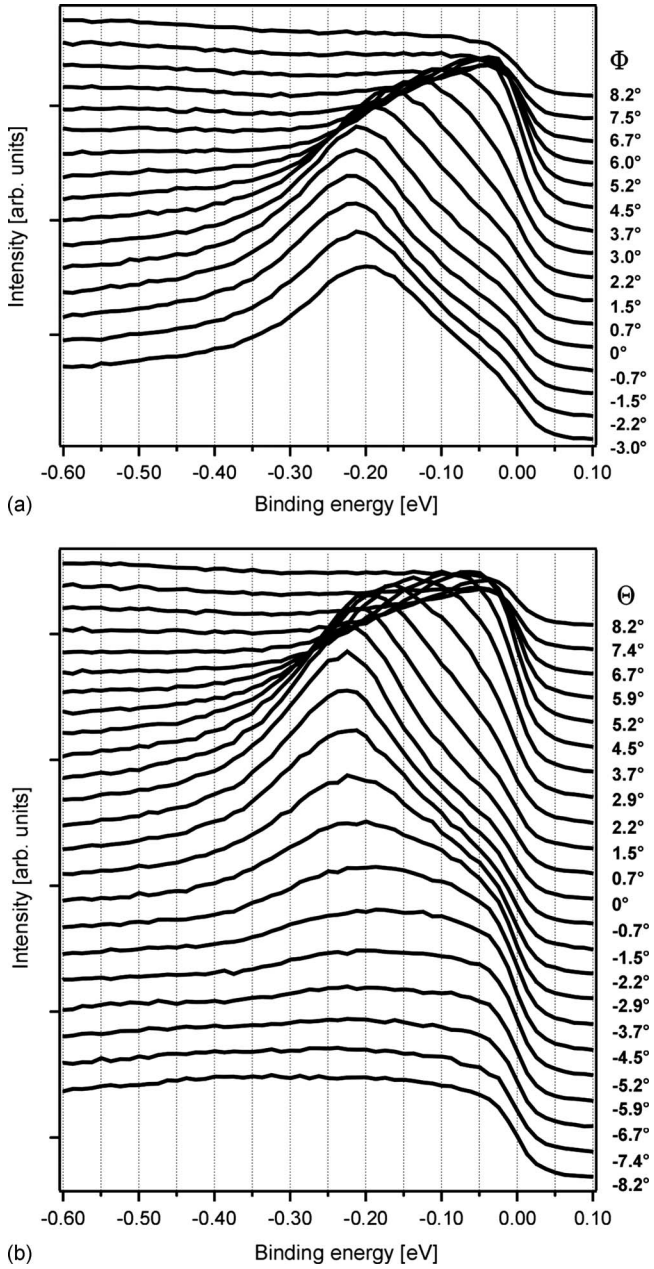

FIG. 9. ARPES measurements on the (100) surface under variation in the emission angles (a) Φ and (b) Θ ($h\nu$=19 eV).

emission angle or photon energy (see Ref. 49 and references therein).

For a quantitative analysis of the ARPES spectra a constant background as determined from the energy region of unoccupied states has been subtracted. To correct intensity variations caused by different emission angles, the spectra were normalized to this background. The intensity dependence on $h\nu$ is considered by normalization with the average total intensity of all spectra taken at one certain photon energy. The work function has been determined by very low energy electron diffraction measurements to $\phi = 5.15 \pm 0.3$ eV.[51] The final electron states are supposed to be free-electron-like. The two following methods are used to extract the Fermi vectors from the ARPES data:

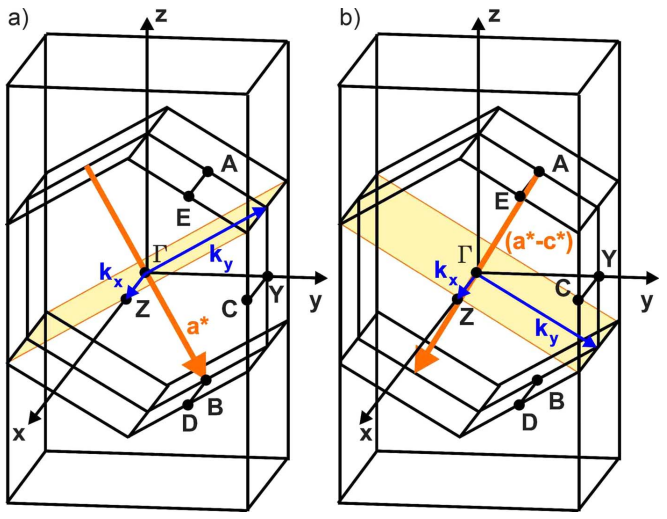

FIG. 10. (Color online) **k**-space cuts corresponding to $\mathbf{k}_\parallel$ measurements in the (a) (100) surface and (b) $(10\bar{1})$ surface. The spherical curvature of the area in ARPES measurements is neglected.

(1) The photoemission intensity is integrated over a 120 meV wide energy region near E_F. The maxima of this integrated intensity $I(\mathbf{k})$ define the Fermi vectors.

(2) Since the Fermi surface is determined by strong variations in the intensity distribution $I(\mathbf{k})$, the gradient $|\nabla_{\mathbf{k}} I(\mathbf{k})|$ could be likewise used to define the Fermi vectors.[52,53] However, this gradient method generally produces two Fermi contour lines. Whereas the contour line on the unoccupied side of the Fermi surface coincides with the real Fermi surface, the other line is an artifact of this technique.[52]

Both methods can be found in the literature. However, the gradient method often results in a better agreement with theoretical predictions.[52]

3. *Fermi surface scans perpendicular to the direction* $\mathbf{a}^*$

In the following, ARPES $\mathbf{k}_\parallel$ scans on the (100) surface will be presented, which allow for a Fermi surface mapping of planes perpendicular to the direction $\mathbf{a}^*$. Such Fermi surface maps can be performed by variation in both emission angles at a fixed photon energy. They provide spherical cuts through **k** space. Nevertheless, for representation reasons, flat projections of the spherical paths are shown. The theoretical data are produced in complete analogy: spherical paths in **k** space are calculated, but flat projections are shown. In order to simplify the discussion, we define a Cartesian coordinate system within the plane of the projection by k_x and k_y, which are the components of the vector $\mathbf{k}_\parallel$ parallel and perpendicular to the direction Γ-*Z*, respectively. This situation is sketched in Fig. 10(a).

In Fig. 11(a), an ARPES $\mathbf{k}_\parallel$ scan through the Fermi body of MoO_2 is displayed. The measurement has been performed at a photon energy of $h\nu$=19 eV. The photoemission intensity at E_F is plotted as a function of k_x and k_y using the intensity method (method 1). Two different Fermi surface structures, characterized by an enhanced photoemission intensity, can be identified, which are marked by solid (red) lines. Most prominent is the ellipsoidal structure, which is

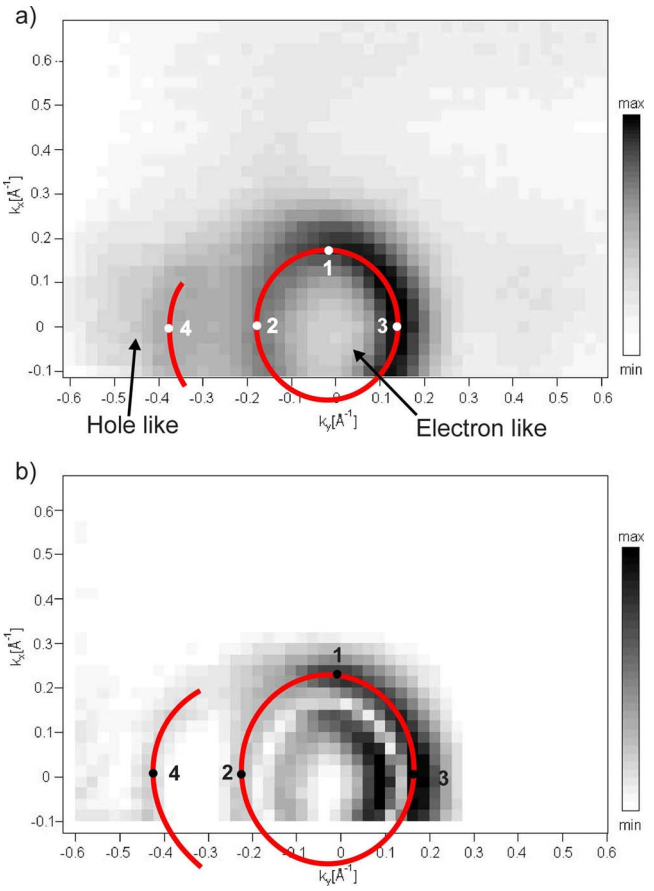

FIG. 11. (Color online) $\mathbf{k}_\parallel$ mapping of the (a) photoemission intensity $I(\mathbf{k})$ at E_F and (b) gradient of the photoemission intensity $|\nabla_{\mathbf{k}} I(\mathbf{k})|$ at E_F, both resulting from an ARPES measurement on the (100) surface taken at a photon energy of $h\nu$=19 eV. Solid (red) lines point to structures of maximal intensity. Points 1–4 mark the Fermi vectors in direction of k_x and k_y.

located around the origin and characterized by points 1–3 with components k_{xF1}=0.175 Å^{-1}, k_{yF2}=−0.175 Å^{-1}, and k_{yF3}=0.150 Å^{-1}, respectively. In addition to this electronlike Fermi surface a much less pronounced holelike Fermi surface contour is observed, albeit for negative values of k_y only. It comprises point 4 with component k_{yF4}= −0.375 Å^{-1} and separates electronlike states with $k_y > k_{yF4}$ from holelike states in the outer region $k_y < k_{yF4}$.

Figure 11(b) shows the photoemission intensity gradient $|\nabla_{\mathbf{k}} I(\mathbf{k})|$ as a function of k_x and k_y (method 2) based on the data shown in Fig. 11(a). In Fig. 11(b), the above-mentioned double structure of the gradient method is nicely visible for the electronlike Fermi surface centered around the origin. The real Fermi surface contours, i.e., those not caused by the artifact of the gradient method, are marked by solid (red) lines. The extent of this Fermi surface amounts to k_{xF1} =0.225 Å^{-1}, k_{yF2}=−0.213 Å^{-1}, and k_{yF3}=0.188 Å^{-1}. The holelike Fermi surface contour for negative values of k_y is also observed in Fig. 11(b). However, the photoemission gradient in this region is very small and, hence, the expected double Fermi surface structure cannot be detected. Only the real Fermi surface contour is visible. The extent of the holelike Fermi surface amounts to k_{yF4}=−0.438 Å^{-1}. In general,

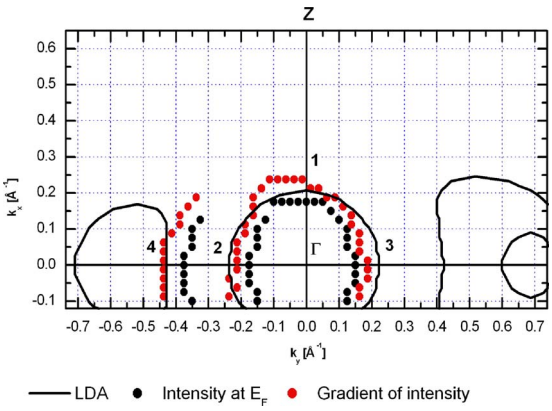

FIG. 12. (Color online) Cut through the Fermi body perpendicular to $\mathbf{a}^*$: ARPES and LDA Fermi surface contours.

the error of both methods of Fermi surface determination is defined by the $\mathbf{k}$ resolution of the ARPES experiment and amounts to $|\Delta\mathbf{k}| \approx 0.025$ Å^{-1}.

In Fig. 12, the experimental ARPES Fermi surface contours as resulting from both the use of the intensity at E_F and the gradient of the intensity are compared to the contours resulting from the LDA calculations. As mentioned above, the LDA calculations are performed on spherical paths, so as to account for the spherical curvature of the experimental plane. However, in the figures, the flat projection on the plane perpendicular to $\mathbf{a}^*$ is shown. Only the $\mathbf{k}$-space region accessible by the ARPES apparatus is included.

According to Fig. 12, the LDA calculations predict an electronlike elliptic Fermi surface around the Γ point. Note that, as will be shown later, $k_\perp$ reaches the Γ point right at $h\nu \approx 19$ eV. As a consequence, the $\mathbf{k}_\parallel$ mappings shown in Figs. 11(a) and 11(b), as well as in Fig. 12, cover a plane perpendicular to $\mathbf{a}^*$, which includes the Γ point [see Fig. 10(a)]. The theoretical findings are confirmed by the ARPES measurements. However, as compared to the LDA results, the Fermi surface contours determined by the intensity method are shifted toward the occupied states. Hence, the ARPES Fermi surface is smaller than the calculated one with the deviations of the measured Fermi vectors ranging from −5% to −32%. Here and in the following all deviations are given with respect to the calculated values. In contrast, the gradient method produces smaller shifts in both directions, away from as well as toward the occupied states. In this case, the deviations of the measured from the calculated values range from −15% to 20%.

Perpendicular to the Γ-Z direction, cuts through two holelike Fermi surface sheets centered around the Y point are predicted by theory [see also Fig. 7(a)]. However, owing to the spherical curvature of the measurement plane, observation of both holelike Fermi surface contours is expected only for positive values of k_y. In contrast, for $k_y < 0$ only one of these contours is cut by the measurement plane, which is indeed observed in the ARPES experiments. In the region of negative k_y its inner surface can be seen in Fig. 12, while both the outer part in $k_y < 0$ and the two holelike structures for $k_y > 0$ are not detected. Compared to the LDA calculations, also the holelike ARPES Fermi surface contour shows a slight shift, which, for the results obtained by the intensity

TABLE I. Magnitudes of Fermi vectors in inverse Å. The experimental Fermi vectors are taken from $\mathbf{k}_\parallel$ scans on the (100) surface ($h\nu$=19 eV) and analyzed using both the intensity maximum and its gradient. The last lines give the respective deviations of the experimental result as based on the gradient method from those arising from the LDA calculations. The plane perpendicular to $\mathbf{a}^*$ through the Γ point has been analyzed. Points 1–4 are marked in Fig. 12.

	$k_{x,F}$	$k_{y,F}$		$k_{y,F}$
	Point 1	Point 2	Point 3	Point 4
		Ellipse		
$I(k)$	0.175	−0.175	0.150	−0.375
$\lvert\nabla_k I(k)\rvert$	0.225	−0.213	0.188	−0.438
LDA	0.207	−0.237	0.222	−0.429
Deviation	9%	−10%	−15%	−2%

method (method 1), is directed toward the occupied states. The corresponding ARPES Fermi surface is thus bigger than the calculated one, and the experimental deviations from the theoretical values amount to 13% to 24%. For the gradient method the ARPES contours generally agree well, but significant shifts with deviations between −2% and 13% are observed near some fractions of the Fermi surface. No systematic trend for the direction of these shifts can be discerned. The experimental and theoretical values of the Fermi vectors k_{xF} and k_{yF} in the plane perpendicular to $\mathbf{a}^*$ through the Γ point as well as the deviations of the theoretical values from the experimental ones as arising from the gradient method are summarized in Table I.

4. Fermi surface scans in the $\mathbf{a}^*\mathbf{c}^*$ *plane*

A variation in $\mathbf{k}_\perp$ can be achieved by varying the photon energy [see Eq. (3)]. In the so-called angle-energy scans one of the emission angles as well as the photon energy $h\nu$ is varied while the respective other emission angle is held constant. From this, Fermi surface scans as a function of $\mathbf{k}_\perp$ and one of the parallel wave vector components (k_x or k_y) can be obtained. In particular, angle-energy scans on the (100) surface under variation in $h\nu$ and the emission angle Θ (variation in k_y) allow a Fermi surface mapping of the $\mathbf{a}^*\mathbf{c}^*$ plane, which is spanned by the vectors $\mathbf{a}^*$ and $\mathbf{c}^*$. With k_x=0 (Φ=0), a cut through the Γ point is achieved. In this situation, $\mathbf{k}_\perp$ is parallel to the direction Γ-*B*, whereas k_y is orientated perpendicular to both Γ-*B* and Γ-*Z*. The thus described cut through the Brillouin zone is sketched in the left column of Fig. 7(a).

The resulting ARPES Fermi surface is given in Fig. 13(a), which shows the intensity $I(\mathbf{k})$ as a function of k_y and $k_\perp$. Both, electronlike and holelike Fermi surface contours can be found, which are marked by light gray (red) and dark gray (blue) points, respectively.

The inner potential, which is necessary for the calculation of $k_\perp$, can be estimated by a comparison of the ARPES Fermi surface contours to the LDA results. The LDA calculations give a peanut-shaped electronlike Fermi surface,

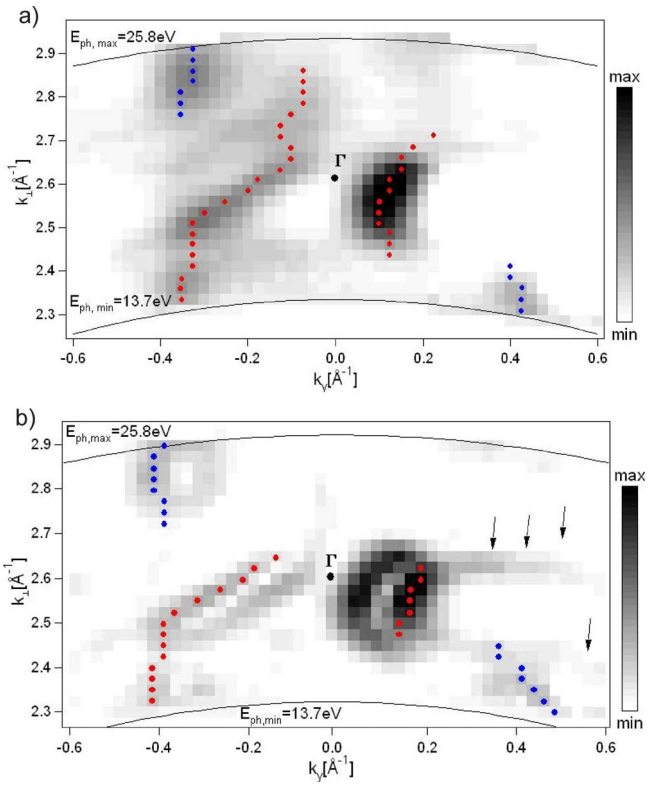

FIG. 13. (Color online) Angle-energy scan on the (100) surface: as a function of k_y and $k_\perp$ (a) the photoemission intensity at E_F, $I(\mathbf{k})$, and (b) the gradient of the photoemission intensity at E_F, $|\nabla_\mathbf{k} I(\mathbf{k})|$, is plotted. Artifacts are marked by arrows. [Light gray (red) points: electronlike Fermi surface contours; dark gray (blue) points: holelike contours].

which is symmetric with respect to the Γ point [see Fig. 7(a)]. This shape is reflected by the ARPES measurements, which likewise display the waist of a peanut of the electronlike Fermi surface. As already mentioned above, the center of this structure, which is just the Γ point, is reached at $h\nu \approx 19$ eV. Using the parabolic free-electron-like final state dispersion (third Brillouin zone), an inner potential of $E_0 \approx -7$ eV is found. This value is comparable to the inner potential defined by the bottom of the valence band in LDA calculations and ARPES measurements ($E_{0,\mathrm{LDA}} \approx -9$ eV).

Figure 13(b) displays the gradient of the intensity, $|\nabla_\mathbf{k} I(\mathbf{k})|$, again as a function of k_y and $k_\perp$ based on the data shown in Fig. 13(a). The typical twofold structure of real Fermi surface contours and the technical artifacts can be observed. The real Fermi surface contours are marked by points. Despite the normalization of the ARPES data, there remain some variations in the photoemission intensity, which are independent of the Fermi surface. In Fig. 13(b), those artificial structures are marked by arrows. They will be neglected in the subsequent discussion.

5. Fermi surface scans perpendicular to the direction ($\mathbf{a}^*$-$\mathbf{c}^*$)

Fermi surface scans have also been performed on the $(10\bar{1})$ surface. If again the spherical curvature of the measurement plane is neglected, the corresponding $\mathbf{k}_\parallel$ scans on

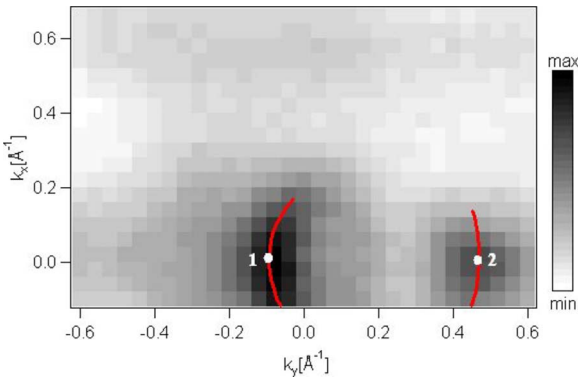

FIG. 14. (Color online) $\mathbf{k}_{\parallel}$ mapping at the $(10\bar{1})$ surface at $h\nu = 19$ eV. The photoemission intensity at E_F, $I(\mathbf{k})$ is plotted as a function of k_x and k_y. The solid (red) lines point up structures of maximal intensity. Points 1 and 2 mark the Fermi vectors in directions of k_x and k_y.

this crystallographic orientation produce cuts through the Fermi body perpendicular to the direction ($\mathbf{a}^*$-$\mathbf{c}^*$) [indicated in Fig. 10(b)]. In particular, while k_x is parallel to the direction Γ-Z, k_y is perpendicular to both the directions Γ-Z and Γ-A. This situation is sketched in Fig. 10(b).

As a matter of fact, ARPES measurements on the $MoO_2(10\bar{1})$ surface lead to less pronounced PES peaks than the measurements on the (100) surface. This might be due to a higher roughness of the surface or an enhanced density of defects.

ARPES $\mathbf{k}_{\parallel}$ scans on the $MoO_2(10\bar{1})$ surface taken at $h\nu = 19$ eV are displayed in Fig. 14, where the intensity $I(\mathbf{k})$ is plotted as a function of k_x and k_y. Near the origin, two separated structures of enhanced photoemission intensity can be observed, which in the direction k_y extent to $k_{yF1} = -0.08$ Å^{-1} and $k_{yF2} = 0.48$ Å^{-1}. In contrast, in the direction k_x no Fermi vector can be defined. The band crossing E_F in point 1 is occupied by electrons in the region $k_y > k_{yF1}$; the band responsible for point 2 is occupied by electrons in the region $k_y < k_{yF2}$. Unfortunately, the photoemission peak creating these Fermi surface contours cannot be observed over the whole range of $k_{yF1} < k_y < k_{yF2}$. As a consequence, it is not clear whether both crossing points are generated by a single band or by two different bands. If they are due to a single band, the region $k_{yF1} < k_y < k_{yF2}$ must be electronlike. Then both Fermi vectors would be part of the calculated peanut-shaped electronlike Fermi surface around the Γ point (see Fig. 7). In contrast, if the crossing points were created by two different bands, only one of the Fermi vectors could be part of the electronlike Fermi surface.

Angle-energy scans on the $(10\bar{1})$ surface allow the investigation of the $\mathbf{a}^*\mathbf{c}^*$ plane [see Fig. 7(a), left column], where $\mathbf{k}_{\perp}$ is in the direction of Γ-A and k_y is orientated perpendicular to both the directions Γ-A and Γ-Z. The corresponding results will be included in the summary plot for the Fermi surface contours in the $\mathbf{a}^*\mathbf{c}^*$ plane to be presented in Sec. III C 6.

6. Fermi surface in the $\mathbf{a}^*\mathbf{c}^*$ *plane: ARPES vs LDA*

So far, different ARPES mappings of the Fermi surface contours of MoO_2 in the $\mathbf{a}^*\mathbf{c}^*$ plane have been described.

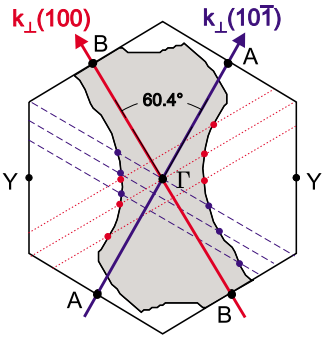

FIG. 15. (Color online) $\mathbf{a}^*\mathbf{c}^*$ plane of the Brillouin zone and of the Fermi body: Angle-energy scans on the (100) and $(10\bar{1})$ surfaces produce cuts perpendicular to the particular $\mathbf{k}_{\perp}$. The end points of the corresponding Fermi vectors are marked by light gray (red) and dark gray (blue) points, respectively.

Furthermore, detailed LDA calculations for this plane have been done. In the following, all these data will be combined into a single representation. To this end, the ARPES results on the $MoO_2(100)$ surface and the theoretical findings can be combined without further treatment. Yet, inclusion of the measurements on the $(10\bar{1})$ surface is more complicated. In a combined plot of results from the (100) and $(10\bar{1})$ surface orientations, the respective Γ points must coincide. Furthermore, since the normal vectors of the (100) and $(10\bar{1})$ surfaces enclose an angle of 60.4°, the perpendicular wave components $\mathbf{k}_{\perp}$ of the two surfaces also have to enclose this angle. The situation is sketched in Fig. 15. For illustration the LDA Fermi surface and some exemplary cuts through the Brillouin zone obtained by angle-energy scans on the two crystallographic surfaces have been included in this figure. However, for each crystal surface there is an uncertainty of the orientation of ±3°. Accordingly, for the angle enclosed by the two surfaces an error of ±6° is supposed.

Of course, in the ideal case, the ARPES findings on the two different crystallographic surfaces of MoO_2 should be consistent among each other and they should be consistent with the LDA calculations. Within the experimental errors, an adjustment of the inner potential E_0, the work function ϕ, and the angle between the perpendicular wave vectors is possible. The best agreement between all experimental and theoretical findings is achieved for an inner potential of $E_0 = -8.5$ eV and a work function of $\phi = 5$ eV for the analysis of the data of the $(10\bar{1})$ surface and an angle of 55.4°. Using these values, we combine all experimental and theoretical Fermi surface results on the $\mathbf{a}^*\mathbf{c}^*$ plane into Fig. 16. Obviously, the overall agreement between the experimental and theoretical findings is very good. Large parts of the theoretically predicted, peanut-shaped, electronlike Fermi surface around the Γ point are observed by the experiment. In particular, the waist of the "peanut" is correctly confirmed by all ARPES measurements. Moreover, the two holelike Fermi surface contours around the Y point can also be observed in the ARPES measurements. Especially at $k_y \approx -0.4$ Å^{-1}, a considerable fraction of this Fermi surface is observed.

Nevertheless, a more detailed analysis between the experimental and theoretical data is hampered by the depen-

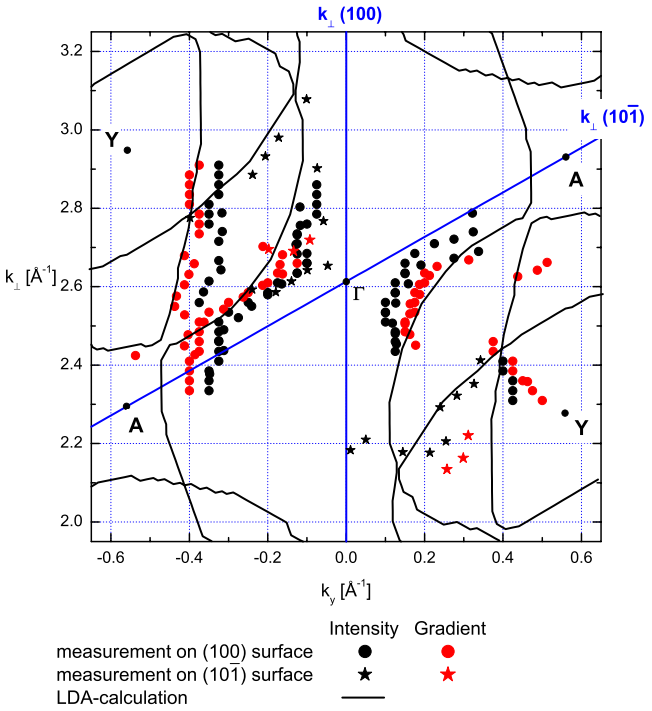

FIG. 16. (Color online) Cut through the Fermi body in the $\mathbf{a}^*\mathbf{c}^*$ plane as indicated in Fig. 15: experimental Fermi surface contours from ARPES measurements on the (100) and (10$\bar{1}$) surfaces and theoretical Fermi surface contours from LDA calculations.

dence of the ARPES results on the method of analysis. Use of the maximal intensity at the Fermi level leads to Fermi surface contours, which compared to the theoretical predictions are shifted toward the occupied states. As a consequence, the corresponding electronlike Fermi surface is smaller; the holelike Fermi surface is bigger than the LDA contours. In general, the deviations are small but the error depends on the absolute size of the Fermi surface and may reach −45% in a few directions. In contrast, analysis of the data with the help of the gradient of the photoemission intensity delivers contours, which agree much better with theory. However, again there exist a few single directions, where the deviations from theory may go up to −30%. Nevertheless, as the comparison of different methods of ARPES data analysis revealed, the gradient method delivers the best results.[52,53] For this reason, only the results of the intensity gradient method will be included in the following discussions.

Finally, in order to allow for a comparison with the de Haas–van Alphen data to be presented in the subsequent section, the ARPES surface area of the electronlike Fermi surface in the $\mathbf{b}^*\mathbf{c}^*$ plane has also been determined and compared to the LDA results. Under the assumption of an ellipsoidal form the area can be calculated using the Fermi vectors in the directions Γ-*Y* (see Fig. 16) and Γ-*Z* (see Fig. 12). As a result, the deviation of the theoretical surface area from the experimental one amounts to −7% (see Table II below).

D. dHvA oscillations

The de Haas–van Alphen effect provides a well-established alternative to study the Fermi surface of metallic systems. This quantum mechanical effect manifests itself as an oscillation of the magnetization/susceptibility as a function of an external magnetic field. The basic ideas of magnetic oscillations in metals were first described by Onsager[54] and later on detailed by Shoenberg.[55]

The periodicity of the oscillations as a function of the inverse of the magnetic field $1/|\mathbf{B}|$ can be associated with a frequency F, which usually is given in units of tesla (T). This frequency F is related to the extremal Fermi surface cross section A_{Fermi} via the Onsager relation,

$$F[\mathrm{T}] = \frac{\hbar}{2\pi e} A_{\text{Fermi}}. \tag{4}$$

Variation in the direction of the magnetic field provides a good guess of the Fermi surface geometry. However, due to the ellipsoidal approximation, which is usually applied to derive the Fermi surface cut from the cross section A_{Fermi}, the shape of the Fermi surface may not be fully resolved. Hence, for more complex Fermi surfaces the evaluation of the data must be complemented, e.g., by LDA calculations. In passing we point to the well-known fact that, in contrast to the ARPES experiments discussed above, de Haas–van Alphen measurements allow us to determine only the extremal cross sections of the Fermi body but do not have access to the complete band structure $E(\mathbf{k})$.

In a more quantitative treatment performed by Lifshitz and Kosevich[56] and Shoenberg[55] the oscillating part of the magnetization parallel to $\mathbf{B}$ is given by the Lifshitz-Kosevich formula,[56]

$$\tilde{M}_{\parallel} \propto \frac{F\sqrt{B}}{\sqrt{A''}} \sum_p R_T R_D R_S \frac{1}{p^{3/2}} \sin\left[2\pi p\left(\frac{F}{B} - \frac{1}{2}\right) \pm \frac{\pi}{4}\right], \tag{5}$$

where $B=|\mathbf{B}|$, $A''=d^2A/dk^2$, R_T, R_D, and R_S are reduction coefficients, and the sum includes all harmonics p.

While a closer investigation of the measured signal reduction delivers more details of the electronic structure, in this paper only the temperature dependent factor R_T is of further interest. A finite temperature T causes a broadening of the Fermi energy, which is reflected by the reduction coefficient,

$$R_T = \frac{X}{\sinh X}, \quad X = \frac{2\pi^2 p k_B T}{\hbar \omega_c}. \tag{6}$$

Finally, via temperature dependent measurements the effective mass m_c of charge carriers included in $\omega_c=(eB/m_c)$ can be determined.

For the dHvA measurements a 15 T magnet system in combination with a ^{3}He/^{4}He dilution refrigerator and a rotator of Oxford Instruments was used. In our setup the field modulation technique was used. Thus the dHvA magnetization is a function of $B_0+b_0\cos(\omega_{\text{mod}}t)$ and was detected via a mutual inductance bridge (astatic coil pair). The measurements were performed at B_0 between 10 and 15 T with a field variation rate of 15 mT/min. The amplitude of the excitation field b_0 was a few millitesla with a modulation frequency of $\omega_{\text{mod}}=19$ Hz. With these values, heating of the specimen by eddy currents can nearly be neglected and the temperature was between 15 and 25 mK.

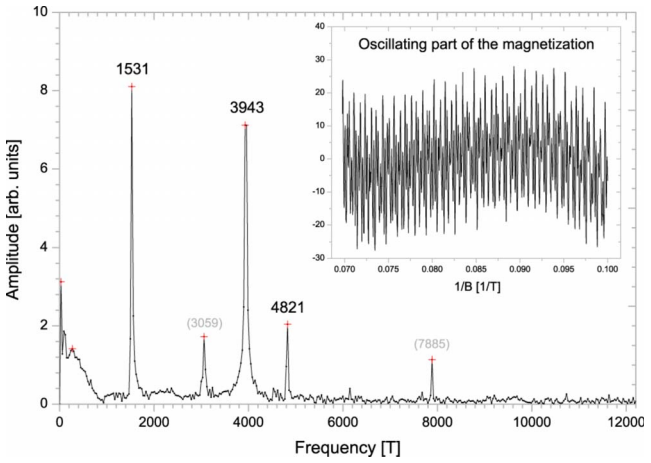

FIG. 17. (Color online) dHvA frequencies of extremal cross sections of the Fermi body in one direction. All extremal cross sections are captured simultaneously (1531, 3943, and 4821 T); higher harmonics are given in brackets (3059 and 7885 T). The inset shows the underlying oscillating part of the magnetization as a function of $1/B$ after subtraction of a third-order polynomial.

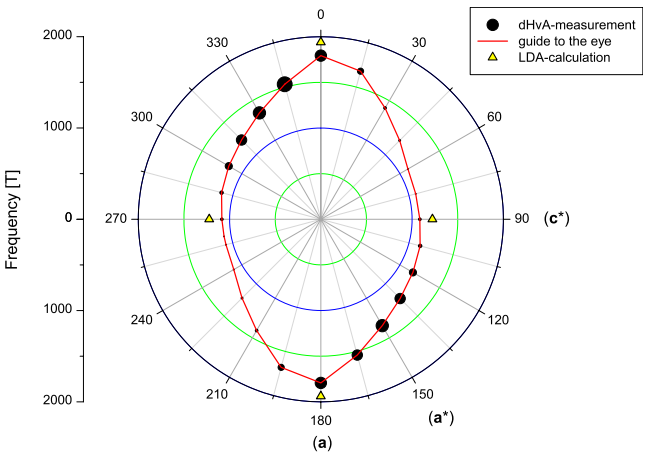

FIG. 18. (Color online) dHvA findings and LDA results of the holelike Fermi surface around the Y point (sheet 1) in the $\mathbf{a}^*\mathbf{c}^*$ plane. The size of the experimental points corresponds to the intensity of the signal.

E. Results (dHvA)

In order to determine the Fermi body of MoO_2, the angular dependence of the dHvA oscillations was measured. With $\mathbf{b}^*$ as the axis of rotation (which is perpendicular to the sheet plane of the following figures) the angle of the magnetic field was varied in the $\mathbf{a}^*\mathbf{c}^*$ plane in steps of 15°. Due to point symmetry the measurements ran only from 345° down to 150° (relative to the **a** axis). To separate the oscillating part of the signal from the background, a third-order polynomial was subtracted from the 2048 points equidistant in $1/B$ (see inset of Fig. 17). A subsequent fast Fourier transformation yielded the frequency spectrum in units of tesla (see Fig. 17). After elimination of higher harmonics and occasional isolated points the angular dependence of the frequencies—and the corresponding mirror points—was plotted in polar coordinates. Each point in the plot represents an area of extremal cross section of the Fermi body. An area in **k** space of 9.55 $\times 10^{-5}$ Å^{-2} corresponds to 1 T. It must be pointed out that all extremal cross sections perpendicular to **B** were captured simultaneously. This complicated the classification of different Fermi surface sheets and of possibly existing multiple extremal cross sections of one Fermi surface sheet. In the $\mathbf{a}^*\mathbf{c}^*$ plane of MoO_2, three different Fermi surface sheets have been detected, which will be treated in detail in Secs. III E 1 and III E 3.

1. dHvA measurement of sheet 1 (Y hole)

In Fig. 18, the angular dependence of the dHvA frequencies of one Fermi surface sheet in the $\mathbf{a}^*\mathbf{c}^*$ plane is plotted. The correlation of the plotted points is well defined by the marginal change in frequency and the relative high intensity. The latter shows a maximum between 120° and 180° caused by a minimal curvature of the area ($\tilde{M}_{\parallel} \propto 1/\sqrt{A''}$). The absence of appreciable intensity between 30° and 75° is an indication of deviations of the rotational symmetry referred to the **a** direction. The deviations can be observed as a small bulge at an angle of 105°. The measured frequency amounts to 1126 T, whereas the frequency at the corresponding angle (with respect to the rotational symmetry) of 255° amounts only to 1076 T. This variation in the magnitude of the bulge in different directions (regarding the whole three-dimensional Fermi surface) can explain differences of the signal intensities. The extension of the dHvA Fermi surface in the $\mathbf{c}^*$ direction (Γ-Y) amounts to 1084 T, in a direction perpendicular to $\mathbf{c}^*$ to 1793 T.

Shape and size of the experimental Fermi surface cross section allow the assignment to one of the LDA Fermi surfaces [see Fig. 7(a)]. The holelike Fermi surface structure centered around the Y point (sheet 1) gives a very similar shape with a bulge at 100°. The size is likewise in good agreement with the results of the calculations. A quantitative comparison can be given for the $\mathbf{c}^*$ direction and the direction perpendicular to $\mathbf{c}^*$. The discrepancies of dHvA extremal surface areas to LDA calculations are -11% in the $\mathbf{c}^*$ direction and -8% perpendicular to $\mathbf{c}^*$. Hence, the experimental dHvA Fermi surfaces are smaller than those theoretically predicted.

2. dHvA measurement of sheet 2 (Y hole)

In Fig. 19, the angular dependence of the dHvA frequencies of a second Fermi surface sheet in the $\mathbf{a}^*\mathbf{c}^*$ plane is shown. The shape of the dHvA Fermi surface resembles the holelike LDA Fermi surface around the Y point, called sheet 2 [see Fig. 7(a)]. However, the contraction of the experimental dHvA Fermi surface in direction of $\mathbf{c}^*$ seems to be smaller than theoretically predicted. Here the deficiencies of the ellipsoidal approximation appear. Perpendicular to the $\mathbf{a}^*\mathbf{c}^*$ plane, in the $\mathbf{b}^*\mathbf{c}^*$ plane, the Fermi surface sheet 2 cannot be described by an ellipsoid. In this plane, the LDA calculations yield a star shaped Fermi surface with an area larger than that of an approximated ellipsoid [see Fig. 7(c)]. The deviations cause less contraction of the measured dHvA Fermi surface in $\mathbf{c}^*$ direction as predicted by theory. The high intensity of the signal at 90° indicates the continuation of the

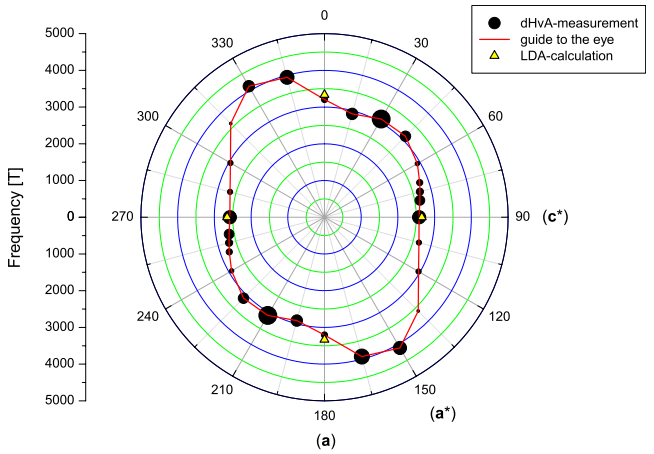

FIG. 19. (Color online) Same as Fig. 18 but for sheet 2 (*Y* hole).

star shape of the $\mathbf{b}^*\mathbf{c}^*$ plane over the whole side.

The measured frequencies amount to 2577 and 3205 T, parallel and perpendicular to the $\mathbf{c}^*$ axis, respectively. These results are −3% and −4% smaller than those predicted by the LDA calculations.

3. dHvA measurement of sheet 3 (electrons)

Figure 20 shows the angular dependence of the dHvA findings of a third Fermi surface sheet in the $\mathbf{a}^*\mathbf{c}^*$ plane. The shape is similar to the electronlike peanut-shaped LDA Fermi surface sheet 3 [see Fig. 7(a)]. Although the approximate rotational symmetry with respect to the **a** axis, which was obtained by the LDA calculations [see Fig. 7(c)], simplifies the identification of the belonging points, there are large changes in frequency combined with weak intensity. The frequency of the peanut waist in direction of $\mathbf{c}^*$ is 1166 T. The discrepancy to LDA calculations amounts to −14%. In the **a** direction a frequency of 5370 T is found. Here the deviation from theory amounts to −10%. Again, the experimental Fermi surface is smaller than the theoretical one. The missing signal at 315° and 330° can be explained by the

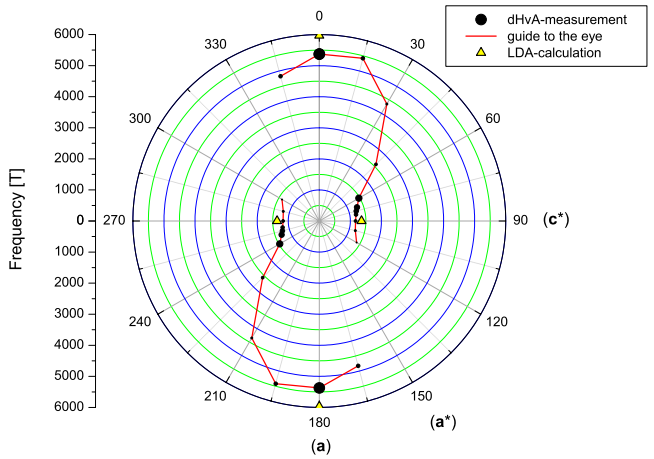

FIG. 20. (Color online) Same as Fig. 18 but for sheet 3 (electron pocket).

open orbits caused by the neck of the peanut in the direction Γ-*B*.

4. Fermi surface in the $\mathbf{a}^*\mathbf{c}^*$ plane: dHvA vs LDA

In the following, the results of the dHvA measurements and the LDA calculations in the $\mathbf{a}^*\mathbf{c}^*$ plane will be compared. In Table II, the dHvA surface areas and the LDA results parallel and perpendicular to $\mathbf{c}^*$ are summarized. All three theoretically predicted Fermi surface sheets have been confirmed by the dHvA measurements. Qualitatively, the shapes of the experimental and theoretical Fermi surface contours agree well.

The quantitative comparison along selected high symmetry directions shows that there are slight discrepancies between the dHvA and the LDA results. All dHvA Fermi surface areas are smaller than calculated by LDA. The discrepancies lie between −3% and −14%. The peanut-shaped electronlike Fermi surface sheet 3 shows the largest deviation to the LDA calculations.

Due to the underlying ellipsoidal approximation, the shape of the dHvA Fermi surface sheets has to be treated with care. For some directions the real Fermi surface topology clearly differs from the assumed ellipsoidal shape. Especially, for sheet 2 (∥ and ⊥ to $\mathbf{c}^*$) and for sheet 3 (⊥ to $\mathbf{c}^*$) the LDA results indicate non-negligible deviations.

A comparison of our dHvA results to previously published magnetotransport data reveals a very good accordance.[22,23,29–31] In particular, the results for the Fermi surface sheet 1 agree nearly perfectly; only differences of less than 1.5% were found. In contrast, only little has been published for sheets 2 and 3. Yet, our results for these Fermi surface sheets, while being much more comprehensive, agree very well with the existing data, the differences being less than 6.5%.

5. Effective masses

Temperature dependent measurements of the magnetic oscillations allow the determination of effective masses of the

TABLE II. Areas of Fermi surface cross sections as resulting from the de Haas–van Alphen measurements and the calculations, respectively. The respective last lines for each sheet give the deviations of the experimental results from the calculated ones. For sheet 3, the corresponding deviation for the ARPES measurements has been added.

		$\parallel\mathbf{c}^*(90°)$	$\perp\mathbf{c}^*(0°)$
Sheet 1	dHvA	1084 T	1793 T
	LDA	1222 T	1939 T
	(dHvA-LDA)/LDA	−11%	−8%
Sheet 2	dHvA	2577 T	3205 T
	LDA	2650 T	3333 T
	(dHvA-LDA)/LDA	−3%	−4%
Sheet 3	dHvA	1166 T	5370 T
	LDA	1358 T	5968 T
	(dHvA-LDA)/LDA	−14%	−10%
	(ARPES-LDA)/LDA	−7%	

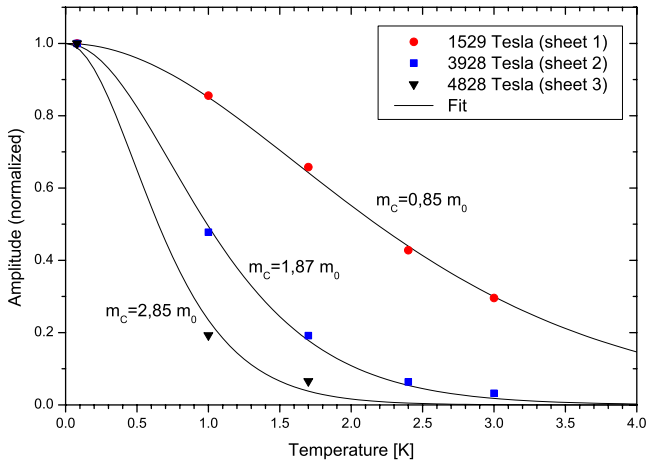

FIG. 21. (Color online) Temperature dependent measurement of the oscillation amplitudes for the three detected Fermi surface sheets and the corresponding effective masses using Eq. (6) as a fit. The angle between **B** and **a** amounts to 75°.

charge carriers via Eq. (6). An increase in temperature causes a reduction in the dHvA signal. For a single orientation of the magnetic field the effective masses of the three observed bands have been analyzed. The angle between **B** and **a** amounts to 75°. The results are displayed in Fig. 21. The temperature has been varied between 0.1 and 3 K. The oscillation amplitudes (normalized to one at $T=0.1$ K) as a function of the temperature are plotted. A fit of the data using Eq. (6) yields the effective masses m_c.

The effective masses of the three Fermi surface sheets differ clearly. Sheet 1 shows a slightly decreased effective mass of $0.85m_0$. However, sheets 2 and 3 exhibit increased masses of $1.87m_0$ and $2.85m_0$, respectively. These values are in good agreement with existing Shubnikov–de Haas measurements.[24] It has to be noted that the described geometry is not the one discussed in conjunction with the ARPES measurements.

IV. DISCUSSION

In general, we found excellent agreement between the experimental and theoretical Fermi surface contours. Both the ARPES and the de Haas–van Alphen results confirm the LDA calculations. In particular, all three Fermi surface sheets predicted by theory have been verified experimentally, with respect to both the shape and the dimensions.

Of course, while from the theoretical side all Fermi surface sheets can be calculated in one go, the measurements are restricted by the respective experimental setups and limitations. For instance, only certain cuts through the Fermi body are usually accessible. In addition, in the ARPES measurements matrix element effects may also play a role, which might undermine the experimental detection of portions of the Fermi surface. This may explain the fact that the calculated Fermi surface contours of all three sheets can only be partially observed by ARPES.

While the overall agreement of the results of all three methods is very good, there still remain small differences on a quantitative level. These deviations have been included in Tables I and II. To be specific, the deviations of the ARPES Fermi vectors from the calculated ones amount to several percent but may go up even to 30% for some experimental points. Yet, both negative and positive deviations occur for both the electronlike and holelike surfaces, precluding systematic errors. This is different for the de Haas–van Alphen measurements. All Fermi surface contours resulting from these experiments, including those given in the literature, are systematically smaller than the calculated ones.[22,23,29–31] To be specific, the electronlike Fermi surface sheet 3 is shifted up to −14% in direction of the occupied states, whereas the holelike Fermi surface sheets 1 and 2 experience a shift of up to −10% in the direction of the unoccupied states. However, we point out that in general the differences between the experimental and theoretical data are of a similar size as the differences between the different experimental techniques.

Nevertheless, all these differences between the experimental and theoretical results, namely, both the unsystematic deviations of the ARPES data and the systematically smaller dHvA Fermi surface contours, still conserve, within the above-mentioned limitations of the experimental setups, the volume of the Fermi body, which, by construction, is correctly accounted for by the calculations.[57]

For the same reason, nonstoichiometry of the samples can most likely be ruled out as a source of the observed quantitative differences. While the phase diagram for Mo-O compounds excludes a hole doping of more than 1.3%,[58] a small defect concentration of 0.12% has been detected by Hall effect measurements.[24] In general, hole doping causes a lowering of the Fermi level. According to the band structure shown in Fig. 6, this is equivalent to a shift of the Fermi surface contours toward the occupied states. However, a shift of up to −30% would necessitate a hole doping of up to 10%. Hence, nonstoichiometry will play only a minor role.

Of course, one might argue that electronic correlations may affect the quality of the calculated results. Indeed, our previous calculations infer the existence of weak electron correlations in MoO_2.[11,20] According to the present measurements, effective masses are only slightly enhanced. Yet, an enhancement may explain the reduction in the bandwidth as it has been observed in the $\mathbf{k}_\parallel$ measurements on the $MoO_2(100)$ surface. However, magnetotransport measurements performed in this direction do not indicate an enhanced effective mass.[23,24,29] Furthermore, as has been demonstrated above part of the experimentally observed bandwidth reduction could be accounted for by the inclusion of the full single-particle potential in the present calculations.

Going into more detail, the deviations between the experimental and theoretical data suggest that, as compared to the experiments, the calculated Fermi body is slightly shortened parallel to the **a** axis and dilated perpendicular to this axis. In the directions perpendicular to **a** this presumption is confirmed by the experimental data. In particular, the cuts through the electronlike ARPES and dHvA Fermi body are smaller than the calculated results. The assumed shortening parallel to **a** is on somewhat weaker grounds. Only the waist of the peanut could be measured by ARPES, but no experimental points exist at the top and bottom of the peanut. In contrast, the dHvA measurements in the direction parallel to

a might be affected by the underlying ellipsoidal approximation. Yet, our assumption is well supported by the overall conservation of the volume of the enclosed Fermi surface as discussed above. Nevertheless, in passing we mention that these deviations are of the order of a few percent only.

V. SUMMARY

A detailed and comprehensive study of the electronic properties of MoO_2 has been presented. This material has been analyzed using angle-resolved photoelectron spectroscopy (ARPES), de Haas-van Alphen (dHvA) measurements, and electronic structure calculations based on a recent full-potential implementation of the augmented spherical wave (ASW) method. The Fermi surfaces determined by both kinds of experiments are in very good agreement with the theoretical predictions. In particular, three different Fermi surface sheets are correctly identified by all three approaches. These sheets include an electronlike peanut-shaped Fermi surface centered around the Γ point, which has a volume of 11% of the Brillouin zone, and two smaller holelike Fermi surfaces both centered around the *Y* point.

As far as they can be detected within the limitations of the experimental geometries, slight differences between the experimental and theoretical results concern mainly the shape of the three Fermi bodies. To be specific, from the calculations the peanut-shaped Fermi body appears to be slightly shortened and elongated parallel and perpendicular to the **a** axis.

With the help of the new calculations, controversies concerning two additional Fermi surface sheets centered around the *Z* and *B* points could eventually be resolved. In particular, the occurrence of these sheets could be attributed to the atomic-sphere approximation, which was used in our previous work. In contrast, in the full-potential ASW calculations, these additional sheets no longer appear. Furthermore, the full-potential treatment led to a much improved agreement between the ARPES results and the calculations as concerns the occupied bandwidth at the Γ point.

In general, the very good agreement between the results obtained by the ARPES and dHvA measurements for metallic MoO_2 has important consequences for the investigation of those neighboring transition-metal dioxides, which display a metal-insulator transition. While the Fermi surfaces of the metallic phases of these materials are not accessible to a low-temperature technique as dHvA experiments, the good agreement found in the present study implies that ARPES measurements will be useful to study the Fermi surfaces of the high-temperature metallic phases.

Furthermore, the good agreement between the different experimental techniques and the electronic structure calculations, with the deviations between measured and calculated data being of the same order as those between the different experimental techniques, supports our original proposal that these calculations are well suited to study the electronic properties of the early transition-metal dioxides. In particular, our results are very encouraging concerning the validity of our calculations for the d^1 members VO_2 and NbO_2 and support the interpretation of the metal-insulator transitions of the latter two compounds as embedded Peierls-type instabilities.

ACKNOWLEDGMENTS

Many useful discussions with K.-H. Höck, R. Horny, G. Obermeier, and S. Klimm are gratefully acknowledged. Thanks are also due to S. G. Ebbinghaus for performing the XRD measurements. This work was supported by the Deutsche Forschungsgemeinschaft through SFB 484 and the European Community through Access to Research Infrastructures (ARI).

*Corresponding author: eyert@physik.uni- augsburg.de

[1] F. J. Morin, Phys. Rev. Lett. **3**, 34 (1959).
[2] G. Andersson, Acta Chem. Scand. (1947-1973) **10**, 623 (1956).
[3] J. M. Longo and P. Kierkegaard, Acta Chem. Scand. (1947-1973) **24**, 420 (1970).
[4] J. B. Goodenough, in *Progress in Solid State Chemistry*, edited by H. Reiss (Pergamon, Oxford, 1971), pp. 145–399.
[5] J. B. Goodenough, Phys. Rev. **117**, 1442 (1960).
[6] D. Adler and H. Brooks, Phys. Rev. **155**, 826 (1967).
[7] D. Adler, J. Feinleib, H. Brooks, and W. Paul, Phys. Rev. **155**, 851 (1967).
[8] A. Zylbersztejn and N. F. Mott, Phys. Rev. B **11**, 4383 (1975).
[9] T. M. Rice, H. Launois, and J. P. Pouget, Phys. Rev. Lett. **73**, 3042 (1994).
[10] R. M. Wentzcovitch, W. W. Schulz, and P. B. Allen, Phys. Rev. Lett. **72**, 3389 (1994).
[11] V. Eyert, Habilitation thesis, Universität Augsburg, 1998.
[12] V. Eyert, Ann. Phys. **11**, 650 (2002).
[13] S. Biermann, A. Poteryaev, A. I. Lichtenstein, and A. Georges, Phys. Rev. Lett. **94**, 026404 (2005).
[14] D. B. Rogers, R. D. Shannon, A. W. Sleight, and J. L. Gillson, Inorg. Chem. **8**, 841 (1969).
[15] R. F. Janninck and D. H. Whitmore, J. Phys. Chem. Solids **27**, 1183 (1966).
[16] T. Sakata, K. Sakata, and I. Nishida, Phys. Status Solidi **20**, K155 (1967).
[17] B.-O. Marinder, Ark. Kemi **19**, 435 (1962).
[18] A. K. Cheetham and C. N. R. Rao, Acta Cryst. B **32**, 1579 (1976).
[19] R. Pynn, J. D. Axe, and R. Thomas, Phys. Rev. B **13**, 2965 (1976).
[20] V. Eyert, R. Horny, K.-H. Höck, and S. Horn, J. Phys.: Condens. Matter **12**, 4923 (2000).
[21] V. Eyert, Europhys. Lett. **58**, 851 (2002).
[22] E. P. Vol'skiĭ and V. M. Teplinskiĭ, JETP Lett. **13**, 340 (1971).
[23] E. P. Vol'skiĭ and V. M. Teplinskiĭ, Sov. Phys. JETP **36**, 550 (1973).
[24] S. Klimm, Ph.D. thesis, Universität Augsburg, 1997.
[25] N. Beatham and A. F. Orchard, J. Electron Spectrosc. Relat. Phenom. **16**, 77 (1979).

[26] F. Werfel and E. Minni, J. Phys. C **16**, 6091 (1983).
[27] R. Prakash, D. M. Phase, R. J. Choudhary, and R. Kumar, J. Appl. Phys. **103**, 043712 (2008).
[28] R. Prakash, R. J. Choudhary, and D. M. Phase, J. Phys.: Condens. Matter **20**, 335225 (2008).
[29] E. P. Vol'skiĭ and V. M. Teplinskiĭ, Sov. Phys. JETP **42**, 373 (1976).
[30] E. P. Vol'skiĭ, A. G. Gapotchenko, E. S. Itskevich, and V. M. Teplinskiĭ, Sov. Phys. JETP **49**, 848 (1979).
[31] V. M. Teplinskiĭ, Sov. Phys. JETP **51**, 995 (1980).
[32] P. Hohenberg and W. Kohn, Phys. Rev. **136**, B864 (1964).
[33] W. Kohn and L. J. Sham, Phys. Rev. **140**, A1133 (1965).
[34] V. Eyert, Int. J. Quantum Chem. **77**, 1007 (2000).
[35] V. Eyert, *The Augmented Spherical Wave Method—A Comprehensive Treatment*, Lecture Notes in Physics Vol. 719 (Springer, Berlin, 2007).
[36] V. Eyert and K.-H. Höck, Phys. Rev. B **57**, 12727 (1998).
[37] V. Eyert, J. Comput. Phys. **124**, 271 (1996).
[38] P. E. Blöchl, O. Jepsen, and O. K. Andersen, Phys. Rev. B **49**, 16223 (1994).
[39] V. Eyert (unpublished).
[40] M. S. Methfessel, Phys. Rev. B **38**, 1537 (1988).
[41] A. Magnéli and G. Andersson, Acta Chem. Scand. (1947-1973) **9**, 1378 (1955).
[42] B. G. Brandt and A. C. Skapski, Acta Chem. Scand. (1947-1973) **21**, 661 (1967).
[43] A. Kokalj, Comput. Mater. Sci. **28**, 155 (2003).
[44] H. Paulin, Diploma thesis, Universität Augsburg, 1996.
[45] M. Cardona and L. Ley, *Photoemission in Solids I: General Principles* (Springer, Berlin, Heidelberg, 1978).
[46] M. Cardona and L. Ley, *Photoemission in Solids II: Case Studies* (Springer, Berlin, 1979).
[47] S. Hüfner, *Photoelectron Spectroscopy* (Springer, Berlin, 1995).
[48] A. Damascelli, Phys. Scr. **T109**, 61 (2004).
[49] M. B. Nielsen, Z. Li, S. Lizzit, A. Goldoni, and Ph. Hofmann, J. Phys.: Condens. Matter **15**, 6919 (2003).
[50] S. V. Hoffmann, C. Søndergaard, C. Schultz, Z. Li, and Ph. Hofmann, Nucl. Instrum. Methods Phys. Res. A **523**, 441 (2004).
[51] J. Moosburger-Will, Ph.D. thesis, Universität Augsburg, 2005.
[52] T. Straub, R. Claessen, P. Steiner, S. Hüfner, V. Eyert, K. Friemelt, and E. Bucher, Phys. Rev. B **55**, 13473 (1997).
[53] L. Kipp, K. Roßnagel, C. Solterbeck, T. Strasser, J. W. Schattke, and M. Skibowski, Phys. Rev. Lett. **83**, 5551 (1999).
[54] L. Onsager, Philos. Mag. **43**, 1006 (1952).
[55] D. Shoenberg, *Magnetic Oscillations in Metals* (Cambridge University Press, Cambridge, 1984).
[56] I. M. Lifshitz and A. M. Kosevich, Sov. Phys. JETP **2**, 636 (1956).
[57] J. M. Luttinger, Phys. Rev. **119**, 1153 (1960).
[58] T. B. Massalski, *Binary Alloy Phase Diagrams*, Vol. 3 (ASM International, Materials Park, 1990).